

See discussions, stats, and author profiles for this publication at: <https://www.researchgate.net/publication/241349765>

# Simulations of Sample-Up-The-Ramp for Space-Based Observations of Faint Sources

Article in *Proceedings of SPIE - The International Society for Optical Engineering* · August 2008

DOI: 10.1117/12.789976

---

CITATIONS

6

READS

1,662

3 authors, including:



**D. J. Benford**

NASA

455 PUBLICATIONS 16,013 CITATIONS

SEE PROFILE

Some of the authors of this publication are also working on these related projects:



PIPER Experiment [View project](#)



BETTII [View project](#)

# Simulations of Sample-Up-The-Ramp for Space-Based Observations of Faint Sources

Dominic J. Benford<sup>†A</sup>, Tod R. Lauer<sup>B</sup>, D. Brent Mott<sup>A</sup>

<sup>A</sup>NASA / Goddard Space Flight Center, Greenbelt, MD 20771 USA;

<sup>B</sup>NOAO, P.O. Box 26732, Tucson, AZ 85726 USA

## ABSTRACT

We have conducted simulations of a memory-efficient up-the-ramp sampling algorithm for infrared detector arrays. Our simulations use realistic sky models of galaxy brightness, shapes, and distributions, and include the contributions of zodiacal light and cosmic rays. A simulated readout is based on the HAWAII-2RG arrays, and includes read noise, dark current, KTC noise, reset anomaly, persistence, and random telegraph noise. The up-the-ramp algorithm rejects cosmic rays, RTN, and KTC noise. The reset anomaly and persistence are also correctable. It produces a best estimate of the source flux under the assumption of very low signal-to-noise, while the overall dynamic range is increased. We present an analysis of the fidelity of image brightness recovery with this algorithm. This work is motivated by the need for sensitive, precise, accurate photometry for Destiny, a mission concept under study for the Joint Dark Energy Mission (JDEM).

**Keywords:** detector readout, infrared space telescope, infrared array, up-the-ramp sampling, dark energy, JDEM

## 1. INTRODUCTION

The authors have been studying the question of multiple sampling, image compression, and cosmic-ray identification and mitigation in the context of processing data for the Destiny<sup>1</sup> mission concept for the Joint Dark Energy Mission (JDEM). The high radiation L2 environment proposed for Destiny, large focal plane array, and need for very low effective read noise to maximize sensitivity require a mature algorithmic approach for on-board processing of the science detector data. While this work was motivated by Destiny's requirements, the method and results presented here are not specific to Destiny and may be applied to other instruments and observatories.

One of the desires, to reduce the read noise, is the subject of a well-established body of work (including the well-known case of Fowler<sup>2</sup> sampling). With detectors featuring a nondestructive readout, where the value of electrons in a pixel can be sampled multiple times between resets, the multiple estimates of the number of electrons reduces the readout error. However, multiple sampling systems have additionally computational complexity. Another desire, image compression, is in this case the desire to coadd signals on-board so as to reduce the data volume to be transmitted. These two desires could be achieved simultaneously and simply, merely by reading and storing the value of each pixel over a set of frames. A reset is triggered between each set of frames, when other instrument or observatory operations (e.g., changing a filter, dithering the image, or pointing to a new position) could be conducted. At the end, the frames are appropriately averaged to result in a single image with improved signal-to-noise and smaller data volume than the original set.

The third desire, to remove cosmic rays, is of particular importance to large-area detectors in space, particularly far from the Earth's magnetic shielding. It is possible for the average of all cosmic rays to be the largest contaminant to the data, but rather than being simply distributed, it is far from either uniform (such as zodiacal light over a typical field of view) or Gaussian (such as photon shot noise); it tends to be dominated by glitches with a large, possibly even saturating, influence on a single or few neighboring pixels. The most straightforward method for the removal of cosmic rays is to read out the detector array multiple times, discard pixels in frames whose value is significantly different from the value at the same pixel at other frames, and co-add the resulting images. For detector arrays that can be sampled nondestructively, multiple reads without resetting the array provides a more sophisticated option. Over a set of frames originating at a common reset, the value in each pixel should increase linearly with time as a consequence of illumination (either from a celestial source, backgrounds such as zodiacal light, or merely the effective illuminating

---

<sup>†</sup> Dominic Benford: ph: (1) 301.286.8771; Fax: (1) 301.286.1617; e-mail: [Dominic.Benford@nasa.gov](mailto:Dominic.Benford@nasa.gov)

signal from dark current). If, at some point in the set, the slope of the increase changes significantly, this indicates the presence of a cosmic ray hit. The act of producing an appropriately-weighted slope estimate also entails the actions of coadding the frames and improving the signal-to-noise as mentioned in the preceding paragraph.

For regularly-spaced samples, a suitable algorithm has been developed<sup>3,4,5</sup> to produce properly weighted coadded slope estimates with cosmic ray rejection. This is known as the sample-up-the-ramp (SUTR) algorithm. We have simplified it slightly and implemented a software simulator to treat certain effects present in the HAWAII-2RG infrared arrays manufactured by Teledyne<sup>6,7</sup>. It should be noted that a SUTR-type approach<sup>3,4</sup> – one in which uniform sampling is used – is superior in efficiency to Fowler sampling<sup>8</sup>, in some cases (saturated sources, bright sources over long integration times) by a factor of  $\approx 2$ .

## 2. SAMPLE-UP-THE-RAMP ALGORITHM DESCRIPTION

Here we describe the SUTR algorithm we have implemented, which draws heavily on the algorithm description given by Offenberget al.<sup>5</sup>, hereafter OFM2005, for memory-efficient up-the-ramp processing. SUTR is based on taking repeated nondestructive samples at equal time intervals from a detector. The value read from each pixel should be approximately a linearly increasing function of time (the “ramp”) whose slope represents the illumination on that pixel. In OFM2005, each individual sample is processed upon arrival, calculating various parameters to enable an appropriately-weighted fit to the data to be calculated upon completion. OFM2005 uses two weighting functions, one of which uses only the two end points (optimized for bright sources) and one of which uses equal weights across all points (optimized for faint sources). This latter case is of most interest for observations requiring the greatest sensitivity, as is the case for Destiny. The weighting function for equal weights is a straight line with sample number, being negative at the beginning and positive at the end to provide a sum of zero to reject any constant offset.

An optimal weighting function must accommodate the actual expected brightnesses of the celestial sources plus any photon background. If the total photon flux in a frame is small compared to the detector read noise for that frame, then the equal weight is optimal. On the other hand, if the reverse is true, then the endpoint weighting is best, although at an effective noise that is worse by about 23%<sup>3</sup>. When these are of similar value, the proper weighting function is somewhere in between, and can be approximated more precisely by, for example, a 3<sup>rd</sup> or 5<sup>th</sup> order polynomial, again subject to the restrictions of symmetry and that the sum be zero. However, this is more computationally complex due to the necessity of calculating and accumulating more weights as each sample is processed. For a canonical 1m aperture, near-infrared, broadband ( $\lambda/\Delta\lambda=5$ ) instrument, the photon noise is equal to the read noise of an H2RG array when observing a point source of magnitude AB~17-19 (depending on readout speed). For observations of sources fainter than this, the equal weighting is best. This brightness is fairly high for deep surveys (for example, the Hubble Ultra Deep Field<sup>9</sup> has a z-band sensitivity limit around 50,000 times fainter than this at AB~30.9). Consequently, we consider the equal weighting to be sufficient for Destiny.

### 2.1 Algorithm Loop

At the beginning of an integration, all digital registers are reset and a single read of a pixel is taken and stored in the variable  $R$ . The loop for the SUTR algorithm begins by setting a variable  $Z$  equal to the previous read stored in  $R$ , then reading a new  $i$ th sample  $R_i$ . In the absence of other events (reset, full well, cosmic ray hit), we increment a counter  $N$  of the number of frames counted since the last event. We must also add to the total signal  $S$  and the weight function  $W$ , which give the least squares fit to the slope  $S/W$ . These are given by:

$$S = \sum_{i=0}^{i=n} R_i \left( i - \frac{n}{2} \right) \text{ and } W = \sum_{i=0}^{i=n} i \left( i - \frac{n}{2} \right) \quad (1)$$

A recursion relation has been determined<sup>5</sup> whereby each value of  $S_i$  and  $W_i$  at sample  $i$  is calculated from:

$$S_i = S_{i-1} + iR_i - \sum_{i'=0}^{i'=i} R_{i'} \text{ and } W_i = W_{i-1} + \frac{i(i+1)}{2} \quad (2)$$

In order to turn the sum in the recursion relation for  $S_i$  into a recursion relation itself, it is evident that the sum merely represents the total of all reads  $R_i$ . A counter for this total,  $T_i$ , is then given by:

$$T_i = T_{i-1} + R_i \text{ so } S_i = S_{i-1} + iR_i - T_{i-1} \quad (3)$$

At each cycle through the loop, a value for  $N_i$ ,  $W_i$ ,  $S_i$ , and  $T_i$  are calculated, and an estimate of the slope,  $S_i/W_i$ , can be made. At the completion of the integration, the last, best, estimate is stored as the value at that pixel. Since this is done consecutively for each pixel of the detector array, a full image is produced by storing arrays of  $N_i$ ,  $W_i$ ,  $S_i$ , and  $T_i$  (Figure 1). Provided the processing can keep up (with typical pixel rates of 100kHz), the image is produced in real time.

The algorithm becomes more complex when considering the full well handling and cosmic ray analysis. In the first case, if the value being read ( $R_i$ ) is found to exceed a pre-determined threshold, then the arrays for  $W_i$  and  $S_i$  are no longer updated and the slope estimate remains that found just prior to reaching the threshold. It is common for detector arrays to feature some nonlinearity while approaching saturation, but to the extent that this effect is stable, it can be measured beforehand and corrected in subsequent post-processing.

For cosmic ray handling, the algorithm has a separate path. At each cycle through the loop, the difference between  $R_i$  and the previous read  $Z$  is calculated and compared to the best estimate slope  $S_i/W_i$ . If it exceeds a pre-determined threshold, then a cosmic ray has been detected. The counter for  $N$  is reset, since new additional weights will be determined for successive reads. A counter  $C_{hit}$  is incremented by 1 and a counter  $C_{size}$  is incremented by the best estimate cosmic ray hit size,  $R-Z - S_i/W_i$ . The total  $T$  is updated to the present value, and the loop continues. An exception to this is if the first pair has an exceptionally large slope, in which case the first sample is discarded.

The algorithm is implemented in IDL<sup>10</sup> to simplify visualization of the results. The variables  $i$ ,  $Z$ , and  $N$  are 16-bit integers, while  $W$ ,  $S$ , and  $T$  are 32-bit integers. This permits up to 512 samples to be taken if the digitization occurs at 16-bit resolution. The data store requires 128 bits per pixel rather than the optimal<sup>5</sup> 107 bits, but using standard data types is more efficient on microcomputers. The algorithm has several input parameters, including total integration time, frame time, single read noise, full well, glitch rejection threshold, KTC noise constant, a sky brightness image, dark current, persistent image, and variables associated with the reset anomaly, cosmic rays, and random telegraph noise. These effects are discussed further in section 3.

## 2.2 Validation of the SUTR Algorithm

In order to ensure that the SUTR algorithm produces accurate images, we conducted a comparative look at three different image restoration approaches. In Figure 2 we show a portion of the Hubble Ultra Deep Field<sup>9</sup> that has been scaled to an appropriate brightness to be seen in a 900 s integration for a large space telescope. In addition to the raw image from HST, there are images produced using the CDS (correlated double sampling), Fowler-8, and SUTR approaches. The assumption in all integrations is a time of 901s, a frame time of 10.6s, and hence a SUTR frame count of 85. By eye, it is possible to see a noticeable improvement of SUTR over Fowler-8, although the difference is slight.

This difference is greatly magnified by including the effects of cosmic ray hits and random telegraph noise, two forms of single-pixel noise terms that can increase overall image variance by a large factor. The SUTR algorithm has its glitch threshold set to a low enough value to detect and remove both effects. It is possible to see by eye again, in Figure 3, that the high noise of cosmic rays eliminates the advantage of Fowler-8 over CDS, but that SUTR continues to perform well. The major feature that can be seen is that there is saturation at the bright star due to the low threshold.

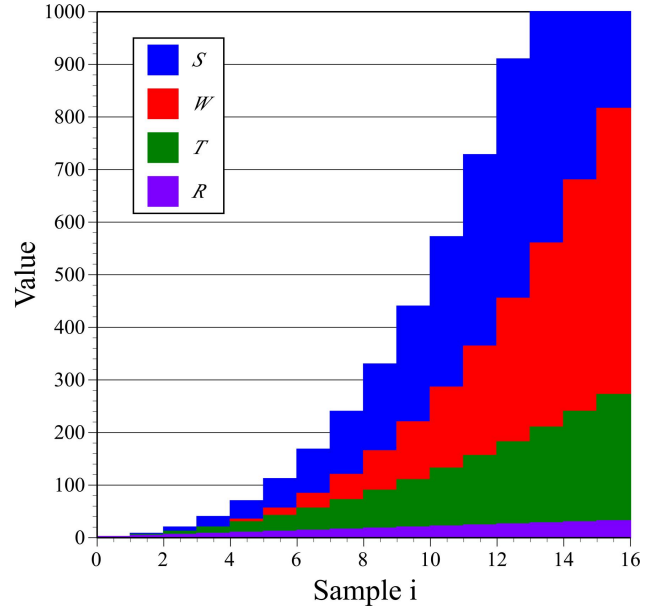


Figure 1. Illustration of the counter values for the sample  $S$ , weight  $W$ , total  $T$  and array read  $R$  for a noiseless pixel of illuminated by a signal of  $2 e^-/\text{frame}$ , all as a function of the frame counter  $i$ .

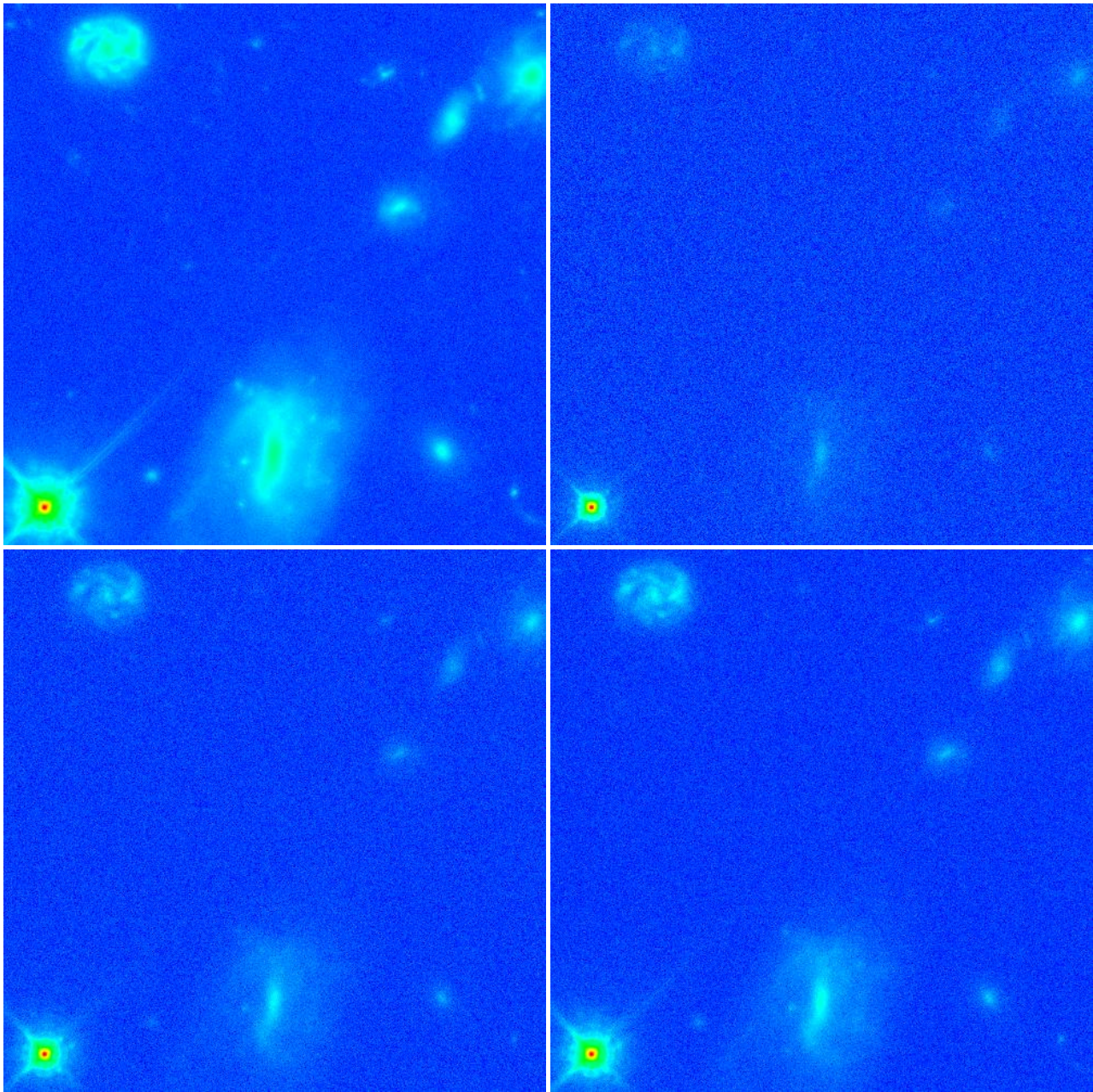


Figure 2. (Upper left) input image from HUDF; (Upper Right) image with CDS after 900s; (Lower left) image processed with Fowler-8; (Lower Right) image processed with SUTR over 900s (85 frames).

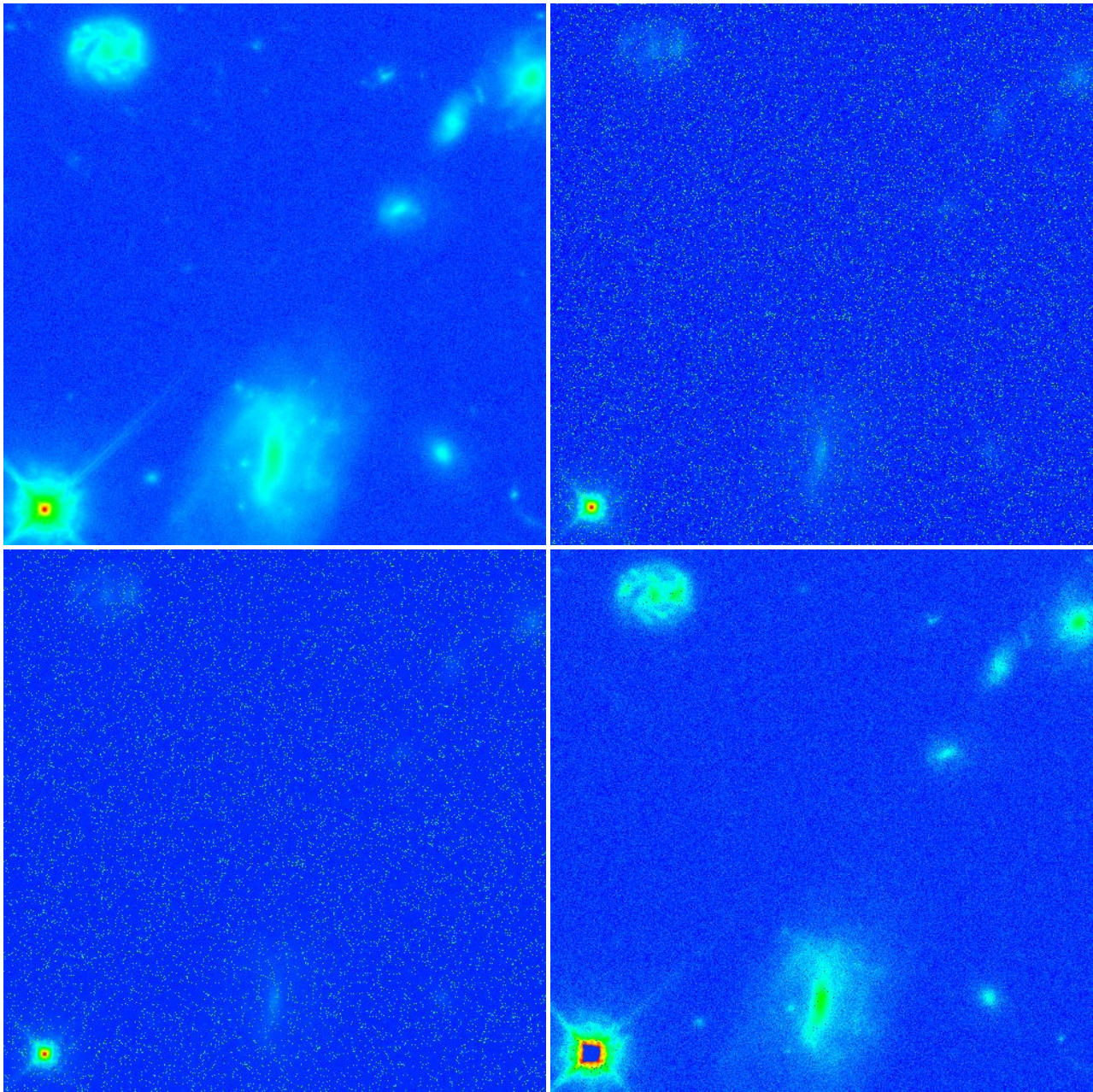


Figure 3. Same frames as in Figure 2, but now including the effects of cosmic rays and random telegraph noise, leading to many speckles in the CDS and Fowler-8 images, and to saturation in the SUTR image due.

### 2.3 SUTR Linearity

To perform a more quantitative analysis of the SUTR algorithm's performance in terms of recovering accurate fluxes, we pursued a Monte Carlo simulation approach. Known fluxes were put into a pixel, SUTR for 901s (85 frames) was performed, and the result checked against the input. A plot of this is shown in Figure 4.

At left is a scatter plot to show the relationship between the output (measured) flux rate and the input. A heavy line is drawn around the scatter region to indicate the  $\pm 3\sigma$  uncertainty expected from read noise. At right is the mean inaccuracy within flux rate bins across the full range. An inaccuracy of  $<1\%$  is achieved over a factor of around one million in flux rate. The point at which full well is reached, presumed to be 60,000 e-, is indicated; accuracy does not change across that threshold. The accuracy plummets when the full well is reached within the first frame, in which case no result is available. The ratio between the final saturation and the full well is thus just the number of frames. Hence, the dynamic range for a given accuracy can be increased by taking frames more quickly or by integrating for longer.

### 2.4 Predictions of Net Noise

Since one of the goals of multiple sampling is to reduce the effective read noise, it is worthwhile ensuring that the algorithm predicts this behavior as expected. A generalized formula for total detector noise is given by Rauscher et al.<sup>11</sup>, from which we can trivially rewrite the portion of read noise appropriate to the SUTR algorithm:

$$\sigma^2_{SUTR} = \frac{12(n-1)}{n(n+1)} \sigma^2_{read}, \quad (4)$$

where  $\sigma_{read}$  is the single read noise and  $n$  the number of frames. At the limit  $n=2$ , the result is merely the CDS read noise at  $\sqrt{2}$  times the single read noise. The effective read noise is predicted to decrease more slowly than  $n^{-1/2}$  at first, approaching the asymptotic behavior of  $\sigma_{read} = 3.46 \cdot n^{-1/2} \cdot \sigma_{read}$  at  $n \sim 10$ . Hence, there is little advantage in using SUTR for short times that result in fewer than  $\sim 10$  frames. If we allow both the intrinsic detector CDS noise and the readout rate to vary, the noise in a fixed 106 second integration time should result in a family of lines as defined by equation 4. This is shown in Figure 5, where Monte Carlo simulations of 16,384 pixels show that the mean noise is very well predicted by the two-parameter formula. Cutting this differently, if we fix the CDS read noise at 25 e- (17.7 e- single read) and instead allow the integration time to vary, we find the result in Figure 6. The integration time must be in multiples of the frame time, and hence the sampling density is nonuniform. Again, theory is validated by agreement with simulation.

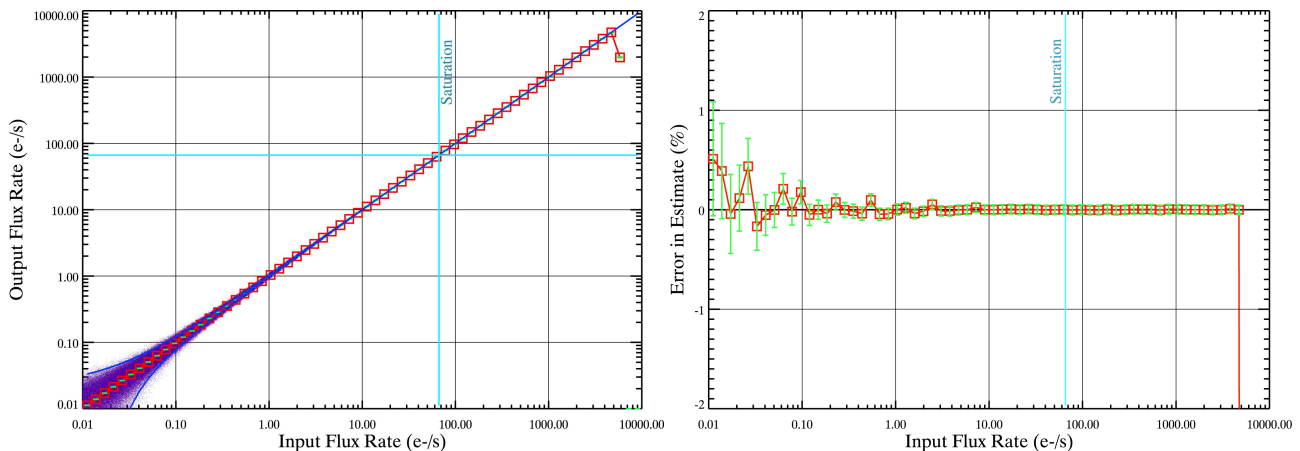


Figure 4. (Left) scatter plot of the output flux found after performing an 85-frame SUTR integration on an input flux. The spreading at the lower left is due to the read noise, the expectation of which is shown by a  $\pm 3\sigma$  boundary drawn over the scatter plot. (Right) Mean inaccuracy of the linearity function for SUTR shows that  $<1\%$  accuracy can be achieved over an input flux range of six decades, corresponding to 15 magnitudes in brightness. The detector full well saturation position is shown in the middle of the linear region; the final divergence from linearity occurs when the detector reaches full well within the first frame. The ratio between final saturation and full well is the number of frames (85).

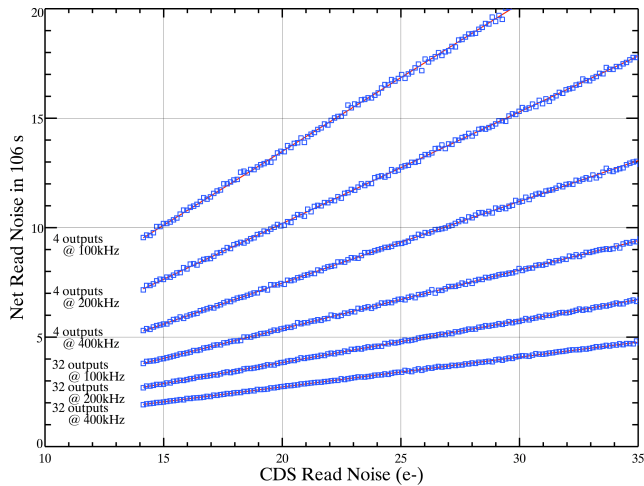


Figure 5. The predicted read noise vs. intrinsic CDS read noise for several sample rates (points) lies perfectly on the prediction (line) of equation 4.

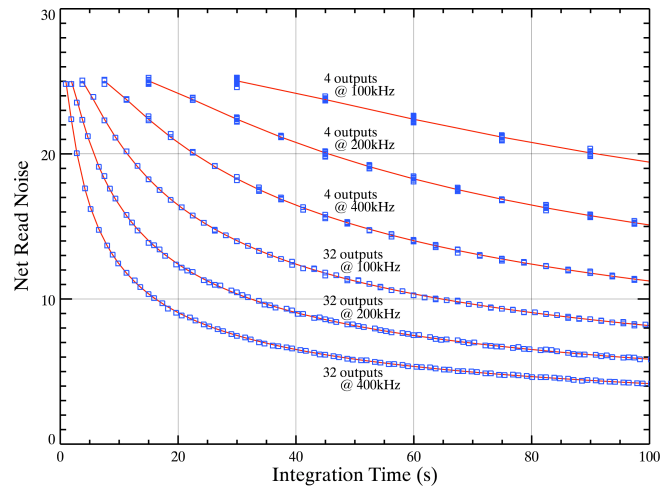
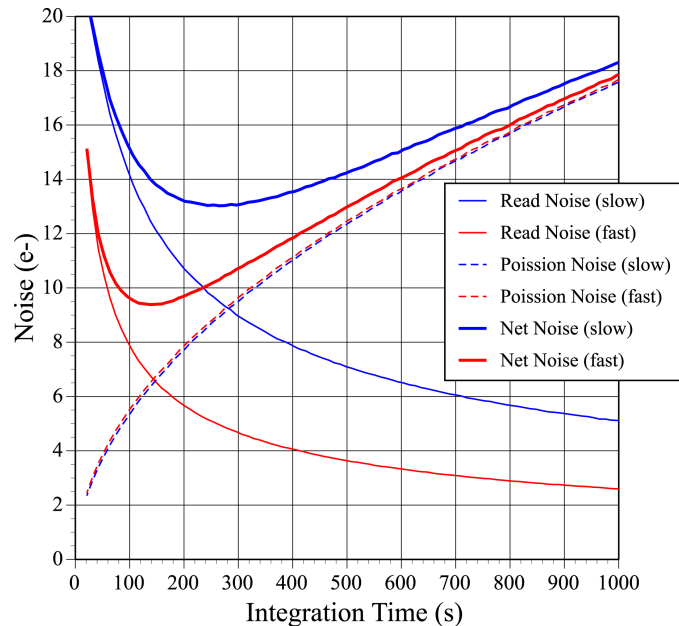


Figure 6. The predicted read noise vs. integration time (actually number of samples) for several sample rates (points) lies perfectly on the prediction (line) of equation 4.

The SUTR simulation software can be used to analyze the different components of total noise. Read noise is discussed above, but photons shot noise and dark current noise also contribute. The difference is that these latter contributions produce Poisson noise that increases with time. There is therefore a tradeoff to be made in readout rate and integration time: instruments should be designed so that the shot noise contributions dominate. Choosing a reasonably faint value of around 0.3 e-/s as a flux rate, we calculate the noise contributions as a function of integration time and readout rate, shown in Figure 7. The rates correspond to roughly 5 s and 1.3 s frame times for the slow and fast rates, respectively.

Figure 7. (At Right) Breakdown of the read noise and Poisson shot noise terms making up the total noise from our SUTR simulation.



### 3. MODELING OF OTHER EFFECTS

#### 3.1 Cosmic Rays

The removal of cosmic rays is, perhaps, the greatest power of the SUTR algorithm. We described the action of the algorithm in section 2.1, and have shown a simulated image of a cosmic-ray-polluted integration in Figure 3. It is worthwhile quantifying how well the cosmic ray removal works in terms of the number of unremoved cosmic rays and change in overall noise in an image. Our cosmic ray model is simple and not necessarily representative of reality, but does provide an approximate distribution that can be compared to the prediction for JWST<sup>12</sup>.

We modeled cosmic rays as events that appear in  $5 \cdot 10^{-5}$  of the pixels in each frame, which corresponds to a cosmic ray rate of around  $200 \text{ cm}^{-2}\text{s}^{-1}$ . This is approximately the predicted (JWST prediction<sup>12</sup>, their figure 13) incident cosmic ray rate in a 200-mil (5.08mm) Al-shielded enclosure.

A simulated blank-field image of cosmic ray rejection is shown in Figure 8. We plot a  $250 \times 250$  pixel region after a 1000 s integration, where on average around 3100 cosmic ray hits should have occurred. Our cosmic ray magnitude is a logarithmically distributed random value between  $10^3$  and  $10^4$  counts. The plot at left is the simulated integration without cosmic rays, and the one in the middle is a raw image with the  $\sim 3100$  cosmic rays. At right is a plot of the SUTR processing of the cosmic rays, showing an image much like the one without cosmic rays. There is only a very slight change in the variance of the two images, and hence it can be inferred that the cosmic ray rejection is nearly perfect. The mean standard deviation is  $13.00 \pm 0.03 \text{ e}^-$  without cosmic rays and  $13.14 \pm 0.04 \text{ e}^-$  with cosmic rays. With 5% of the pixels having a cosmic ray, if we ask what the standard deviation is for those pixels, we see that it is higher –  $15.6 \pm 0.2 \text{ e}^-$  – and so there is some added uncertainty, although clearly much less than what would be present if the cosmic rays were not removed.

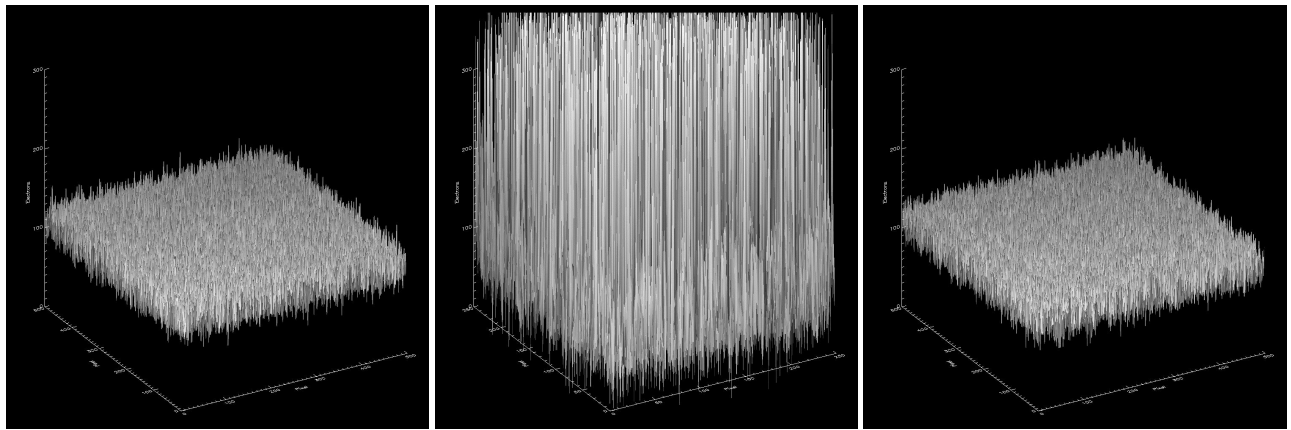


Figure 8. (Left) A SUTR simulation for a uniform flux rate of  $0.1 \text{ e}^-/\text{s}$  with not cosmic rays shows a total of  $100 \text{ e}^-$  after 1000 s, with noise dominated by photon shot noise. (Middle) An identical simulation, but now with cosmic rays that fill  $\sim 5\%$  of the pixels such that their noise dominates. (Right) Finally, a complete SUTR simulation with cosmic rays removed during the processing, where the result looks, by eye, identical to the first. There is a small change in total noise due to a  $\sim 20\%$  excess noise in the pixels from which cosmic rays were removed.

### 3.2 KTC Noise

Each time a pixel is reset, a small random charge must remain. The reason for this is that there are small random thermal currents flowing through the input circuit capacitance during the reset. After the reset switch is opened, whatever charge was there is frozen. The magnitude of this residual charge distribution is termed ‘KTC’ noise as it is given by:

$$\sigma_{KTC} = \frac{\sqrt{kT_{ROIC} C_{Pixel}}}{e^-}, \quad (5)$$

where the read-out integrated circuit temperature is  $T_{ROIC}$  and the total capacitance at a pixel is  $C_{Pixel}$ . For the HAWAII-2 arrays, the value of  $C_{Pixel}$  is of order  $50 \text{ fF}$ <sup>6</sup>, and so at a temperature of 140 K the magnitude of the KTC noise is approximately  $60 \text{ e}^-$ . Fortunately, this is larger than the single read noise, which is perhaps  $35 \text{ e}^-$ . Modeling shows that KTC noise is effectively removed.

### 3.3 Reset Anomaly

The reset anomaly is an apparent excess signal in a detector following reset, which has some of the appearance of increased dark current that slowly tapers off. The effect, which is not seen in all detector pixels, has been discussed in

detail by Rauscher et al.<sup>11</sup>, who found that an exponential fit closely matches their data. In addition, the contribution appears to be stable (i.e., is found not to vary or add noise.) We included the effective signal from reset anomaly into our simulated integration to determine its effect. We made the value large enough (450 electrons amplitude) and with an appropriate timescale (16 s) to be easily visible and nonlinear during the course of an integration. The SUTR slope derived from the measurement of a pixel featuring reset anomaly is incorrect, overestimating the true slope. However, because the effect is noiseless, the same pattern appears in both dark and illuminated frames. The difference image resulting from dark subtraction is therefore free from reset anomaly defects. This is shown in Figure 9.

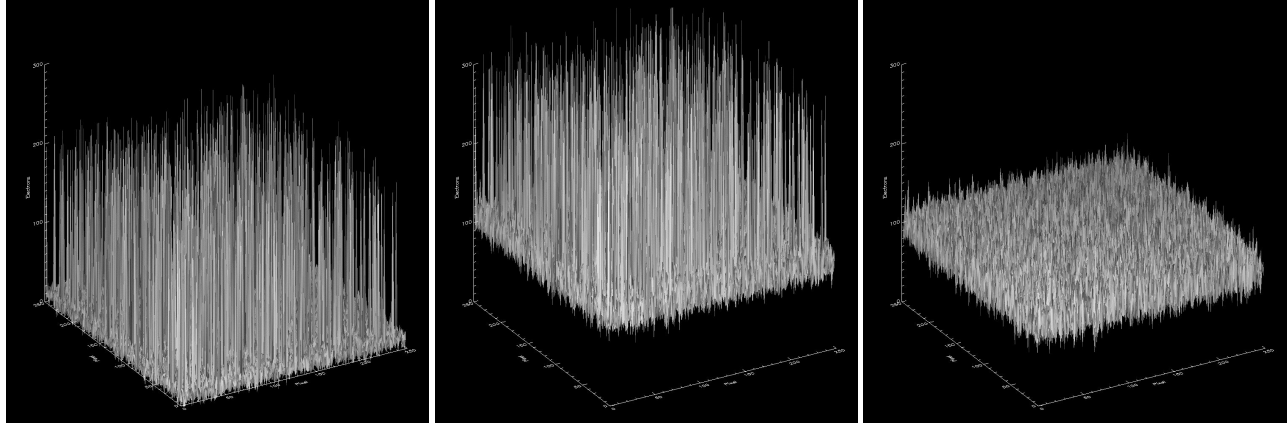


Figure 9. Simulations show that the noiseless reset anomaly can be subtracted out, even when the signal is both strong and nonlinear in many pixels. (Left) a dark frame with 1% of the pixels showing reset anomaly; (Middle) an illuminated frame with the same pixels showing the same reset anomaly; (Right) a differenced image illustrating effective subtraction.

### 3.4 Persistence

Persistence, also called latent charge, is the apparent signal on an unilluminated pixel resulting from exposure to photons at some earlier time. If the detector was exposed to high photon flux levels, for instance several times the saturation flux, processes which, with some delay often extending into hours, release charge into the conduction band can contribute to the signal read out at later times. Persistence is a function of, at least, the (bright) incident flux during a prior exposure and the time elapsed since the exposure.

We have fitted the persistence found during testing of FPA126 (for Wide Field Camera 3), finding that the persistence signal is proportional to  $\exp(-4.1 \cdot t^{0.15})$  where the time  $t$  is in minutes. This effect is included in the SUTR simulation, and we have tested for the accuracy of measuring faint fluxes in the integration immediately after a very bright integration. The magnitude of the effect is such that after a prior frame that had just reached full well, for an integration time of 106 s, the persistent charge rate in the subsequent integration averages around 0.2 e-/s, but the instantaneous rate varies by roughly an order of magnitude over the integration. An offset was taken off the second integration to remove the integrated signal expected after the first, which amounts to a linear correction to the slope measurement. The result is shown in Figure 10.

For the faintest level tested, 1.0 e-/s of flux in the following integration, the slope measurement is accurate to <1% when the charge stored in that pixel during the preceding integration is less than around the full well value. Since the persistent charge at that level is around 0.2 e-/s but the inaccuracy is at the  $\sim 0.01$  e-/s level, it could be said that the SUTR algorithm with the linear correction does reduce the persistence effect by 95%. The prior-integration charge at which inaccuracy due to persistence begins to contribute increases in rough proportion to the increasing flux rate in the second integration, since the fractional contribution of the persistence is smaller. It is interesting to note that the standard deviation behaves similarly, although the curves overlap each other when the persistence becomes the dominant effect. This occurs roughly where the average charge rate from persistence equals the flux rate, or in the 106 s case, where the second-integration flux rate is around  $10^{-6}$  of the first-integration total charge.

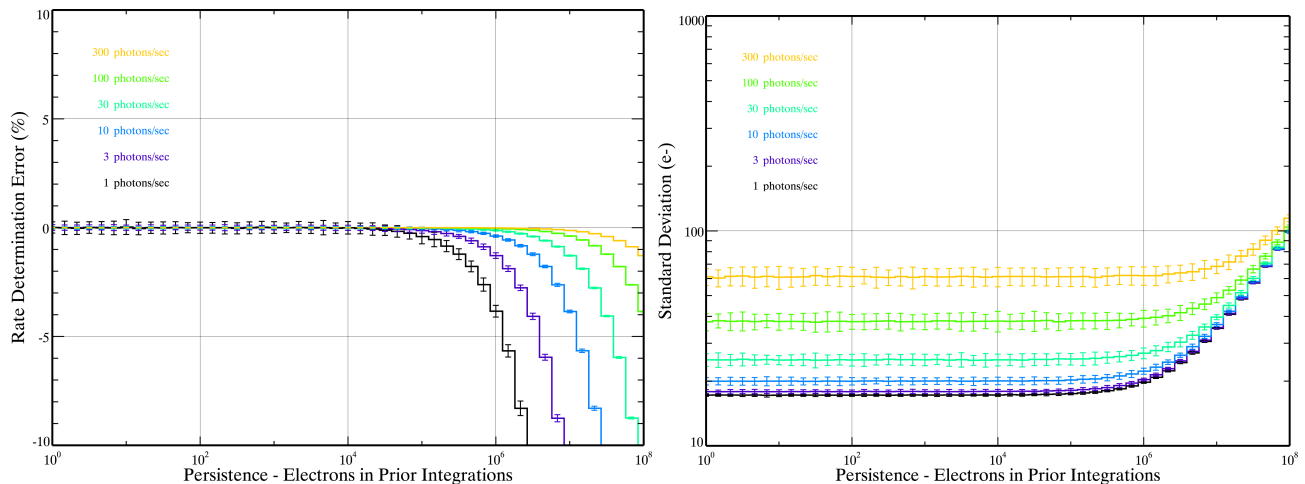


Figure 10. These graphs apply to simulations of the effect of persistence in a 106 s integration after linear calibration. (Left) Rate accuracy for several different flux rates as a function of the number of electrons in the prior frame. A divergence from near-zero error is seen when the persistent electron mean rate becomes comparable to the flux rate, which occurs when the flux rate in e-/s is roughly  $10^{-6}$  of the prior integration charge in e-. (Right) Standard deviations for the simulations, showing that the beginning of inaccuracy occurs where the variance of persistent electrons begins to dominate the variance of new electron shot noise.

### 3.5 Random Telegraph Noise

Large-amplitude RTN is a phenomenon where the detector level will suddenly jump to a new level and then continue behaving normally, and where the magnitude of the jump is large compared to the read noise. Small-amplitude RTN, where the jumps are similar to or smaller than the read noise, are not treated here, as an algorithm to distinguish between an RTN jump and a random read noise event has not been developed. It has been shown<sup>11</sup> for several detector arrays that the RTN occurs in a small and fixed number of pixels in an array, and so may not contribute a significant amount to the variance of an array overall. However, since it is possible for SUTR to handle this effect, we have simulated the algorithm's performance in terms of the mitigation of RTN.

RTN appears as a toggling between two or more levels during an otherwise normal integration. The magnitude and frequency of these toggles varies from pixel to pixel, but a reasonable guess based on the data of Rauscher et al.<sup>11</sup> is that the magnitude of 300 e- and a transition probability of 10% is representative of the effect. We placed RTN at this level into 1% of the pixels and set the cosmic ray removal threshold to capture events that jump by more than  $\sim 175$  e- between successive frames (for perfectly dark frames; an increasingly greater jump is allowed for pixels as the pixels' flux rate becomes comparable to the 175 e- point.) The processing of the SUTR algorithm is sign symmetric, as it operates by comparing variances and slopes squared. Hence, a negative jump is processed in the same way as a positive jump, and the toggling of RTN can be treated with the cosmic ray removal. The time series for a 901 s integration is shown in Figure 11, where the SUTR slope estimate is shown as the line along the bottom of each pixel's series. An arbitrary offset has been added to each channel, although the KTC offset of RMS  $\sim 40$  e- is an appreciable fraction of that offset.

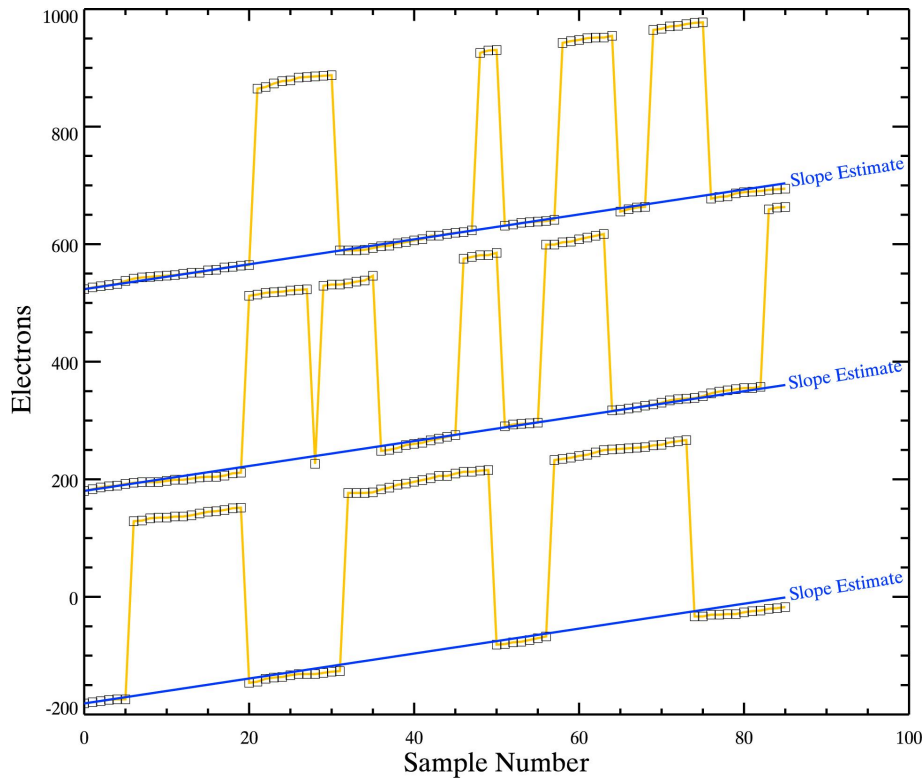


Figure 11. These three time series of 85 frames in a SUTR integration with RTN show that the slope estimate from the SUTR algorithm is robust to the addition of the toggling behavior of RTN. While the recovery is not perfect in the event of smaller RTN amplitude or brighter sources, SUTR does greatly improve the usability of data from affected pixels.

## CONCLUSIONS

Our simulations of a sample-up-the-ramp algorithm for HAWAII-2RG detector arrays have validated several aspects of its performance. It performs linearly with respect to input flux, provides significant data volume reduction as compared to a series of individual frames, and reduces read noise as compared to CDS or Fowler-8 (when the number of frames is more than around 10). Furthermore, the algorithm features excellent suppression of KTC noise, cosmic rays, reset anomaly, and RTN. We found that, for our trial conditions, persistence is reduced by 95%. The SUTR algorithm performs best for faint sources, as is expected to be the case for most science observations for the Destiny mission implementation of JDEM.

## ACKNOWLEDGMENTS

Many thanks are due to Dale Fixsen for discussions of the SUTR algorithm, Bernie Rauscher for his help with the initial simulation, Augustyn Waczynski for kindly taking the FPA126 persistence and other detector data, and several people at Teledyne for their cooperation on understanding detector performance, notably Dave Gulbransen, Dean Menes, Markus Loose, Jim Beletic, and James Garnett. Ian Dell'Antonio provided realistic sky simulations to test SUTR against, and provided motivation to achieve the best results possible.

## REFERENCES

- [1] Benford, D.J. & Lauer, T.R. 2006, Proc. SPIE, Volume 6265 (Space Telescopes and Instrumentation I: Optical, Infrared, and Millimeter), pp. 626528; "*Destiny: a candidate architecture for the Joint Dark Energy Mission*"
- [2] Fowler, A.M. & Gatley, I. 1991, Proc. SPIE, Volume 1541 (Infrared Sensors: Detectors, Electronics, and Signal Processing), pp. 127-133; "*Noise reduction strategy for hybrid IR focal-plane arrays*"
- [3] Fixsen, D.J., Offenber, J.D., Hanisch, R.J., Mather, J.C., Nieto-Santisteban, M.A., Sengupta, R. & Stockman, H.S. 2000, PASP, 112, pp.1350-1359; "*Cosmic-Ray Rejection and Readout Efficiency for Large-Area Arrays*"
- [4] Offenber, J.D., Fixsen, D.J., Rauscher, B.J., Forrest, W.J., Hanisch, R.J., Mather, J.C., McKelvey, M.E., McMurray, R.E., Jr., Nieto-Santisteban, M.A., Pipher, J.L, Sengupta, R. & Stockman, H.S. 2001, PASP, 113, pp. 240-254; "*Validation of Up-the-Ramp Sampling with Cosmic-Ray Rejection on Infrared Detectors*"
- [5] Offenber, J.D., Fixsen, D.J. & Mather, J.C. 2005, PASP, 117, pp.94-103; "*Memory-Efficient Up-the-Ramp Processing with Cosmic-Ray Rejection*"
- [6] Loose, M., Farris, M.C., Garnett, J.D., Hall, D.N.C & Kozlowski, L.J. 2003, Proc. SPIE, Volume 4850 (IR Space Telescopes and Instruments), pp. 867-879; "*HAWAII-2RG: a 2k x 2k CMOS multiplexer for low and high background astronomy applications*"
- [7] Garnett, J.D., Farris, M.C., Wong, S.S., Zandian, M., Hall, D.N., Jacobson, S., Luppino, G., Parker, S., Dorn, D., Franka, S., Freymiller, E. & McMuldloch, S. 2004, Proc. SPIE, Volume 5499 (Optical and Infrared Detectors for Astronomy), pp. 35-46; "*2K X 2K molecular beam epitaxy HgCdTe detectors for the James Webb Space Telescope NIRCcam instrument*"
- [8] Garnett, J.D. & Forrest, E.J. 1993, Proc. SPIE Vol. 1946 (Infrared Detectors and Instrumentation), p. 395-404; "*Multiply sampled read-limited and background-limited noise performance*"
- [9] Hubble Ultra Deep Field web site: <http://www.stsci.edu/hst/udf>
- [10] IDL: Interactive Data Language; web site: <http://rsinc.com/idl/>
- [11] Rauscher, B.J., Fox, O, Ferruit, P., Hill, R.J., Waczynski, A., Wen, Y., Xia-Serafino, W., Mott, B., Alexander, D., Bramabara, C.K., Derro, R., Engler, C., Garrison, M.B., Johnson, T., Manthripragada, S.S., Marsh, .M., Marshall, C., Martineau, R.J., Shakoorzadeh, K.B., Wilson, D., Roher, W.D., Smith, M., Cabelli, C., Garnett, J., Loose, M., Wong-Anglin, S., Zandian, M., Cheng, E., Regan, M.W., Hall, D.N.B., Hodapp, K.W., Böker, T., De Marchi, G., Jakobsen, P & Strada, P. 2007, PASP, 119, pp. 768-786; "*Detectors for the James Webb Space Telescope Near-Infrared Spectrograph. I. Readout Mode, Noise Model, and Calibration Considerations*"
- [12] Barth, J.L., Isaacs, J.C. & Poivey, C. 2000, NGST Report #570, "*The Radiation Environment for the Next Generation Space Telescope*"